PCCP

Deactivation-Free Ethanol Steam Reforming at Nickel-Tipped Carbon Filaments

Journal:	*Physical Chemistry Chemical Physics*
Manuscript ID	CP-ART-02-2021-000637.R2
Article Type:	Paper
Date Submitted by the Author:	02-May-2021
Complete List of Authors:	Mueanngern, Yutichai; The Ohio State University of Department of Chemistry, Chemistry; Personal Li, Cheng-Han; The Ohio State University, Materials Science and Engineering Spelic, Meiling; The Ohio State University of Department of Chemistry, Chemistry Graham, Joshua; The Ohio State University of Department of Chemistry, Chemistry Pimental, Nathan; The Ohio State University of Department of Chemistry, Chemistry Khalifa, Yehia; The Ohio State University of Department of Chemistry, Chemistry Jinschek, Joerg; The Ohio State University, Materials Science and Engineering Baker, Lawrence; Ohio State University, Chemistry and Biochemistry

Deactivation-Free Ethanol Steam Reforming at Nickel-Tipped Carbon Filaments

Yutichai Mueanngern[1], Cheng-Han Li[2], Meiling Spelic[1], Joshua Graham[1], Nathan Pimental[1], Yehia Khalifa[1], Joerg R. Jinschek[2], and L. Robert Baker[1]*

[1] Department of Chemistry and Biochemistry, The Ohio State University, Columbus Ohio 43210, United States.

[2] Department of Materials Science and Engineering, The Ohio State University, Columbus Ohio 43210, United States.

Supporting Information Available

ABSTRACT: Ni based catalysts have been widely studied for H_2 production due to the ability of Ni to break C-C and C-H bonds. In this work, we study inverse catalysts prepared by well-controlled sub-monolayer deposition of CeO_2 nanocubes onto Ni thin films for ethanol steam reforming (ESR). Results show that controlling the coverage of CeO_2 nanocubes on Ni enhances H_2 production by more than an order of magnitude compared to pure Ni. Contrary to the idea that C deposits must be continuously oxidized for sustained H_2 production, the surface of the most active catalysts show significant C deposition, yet no deactivation is observed. HAADF-STEM analysis reveals the formation of carbon filaments (CFILs), which propel Ni particles upward at the filament tips via a catalytic tip growth mechanism, resulting in a Ni@CFIL active phase for ESR. Near-ambient pressure XPS indicates that the Ni@CFIL active phase forms as a result of C gradients at the interface between regions of pure Ni metal and domains of closely packed CeO_2 nanocubes. These results show that the mesoscale morphology of deposited CeO_2 nanocubes is responsible for templating the formation of a Ni@CFIL catalyst, which resists deactivation leading to highly active and stable H_2 production from ethanol.

H_2 production from carbon-based oxygenates such as bioethanol has gained attention as an alternative source of H_2 for fuel-cell applications.(1-4) Noble metal catalysts such as Pt and Pd are commonly used in ethanol steam reforming (ESR) owing to their stability and high catalytic activity towards production of H_2 gas.(5-8) Inexpensive transition metal catalysts supported on an active oxide phase presents an affordable alternative to noble metal catalysts and have been effectively used in ESR with comparable initial activity.(9-15) However, stability against deactivation resulting from C deposition on the active metal surface remains a significant challenge to replacing noble metal catalysts with low-cost, earth-abundant alternatives.(4-11, 13, 16-19)

Several studies have reported enhanced catalytic activity towards H_2 production on Ni/CeO_2 catalysts at relatively mild conditions;(20-22) however, the reaction mechanisms on such catalysts have only recently been investigated using in situ and/or operando methods.(23, 24) For example, Xu et.al employed in situ diffuse reflectance infrared Fourier transform spectroscopy (DRIFTS) to identify acetate, carbonate, hydroxyls, and ethoxy as the primary surface intermediates during ESR.(23) CeO_2 was found to facilitate the oxidation of ethoxy to acetate, whereas Ni was shown to catalyze the dissociation of ethoxy to carbonate and surface methyl groups.(24) Near-ambient pressure X-ray photoelectron spectroscopy (NAP-XPS) studies by Liu et al. further identified Ce^{3+} as the active site for surface hydroxyl formation and metallic Ni^0 as the active site for C-C and C-H bond dissociation.(9) In addition, a NiC_x carbide phase was found to exist at room temperature, which decomposes during reaction leading to coke deposits on the Ni surface.(16) These coke deposits result in rapid deactivation unless

continuously oxidized during the course of the reaction by surface hydroxyls that form on CeO_2 and migrate to Ni.(9, 23)

Even in the cases where Ni/CeO_2 bifunctionality leads to partial coke removal, it is difficult to completely eliminate C accumulation to achieve prolonged H_2 production from alcohol-based feedstocks.(23) In this paper we demonstrate a unique, but effective, approach for stable H_2 production from ethanol using an inverse catalyst prepared by controlled, sub-monolayer deposition of CeO_2 nanocubes onto Ni thin films. ESR on these catalysts results in rapid growth of a dense network of carbon filaments (CFIL) on the Ni/CeO_2 catalyst. Despite rapid C deposition in the form of CFIL, the H_2 production rate is greater than 10-fold higher compared to pure Ni, and we detect no measurable sign of deactivation for reaction times >3 h. We find that the active site for this catalyst is Ni nanoparticles supported at the tips of CFIL (Ni@CFIL). During this process, the Ni@CFIL active phase is continuously propelled upward during filament growth. The byproduct of CFIL growth from ethanol is H_2, which proceeds readily on Ni@CFIL catalysts with no deactivation

To understand the formation of a deactivation-resistant Ni@CFIL active phase for H_2 production, these studies are performed on catalysts consisting of CeO_2 nanocubes deposited on Ni thin films as a function of well-controlled sub-monolayer CeO_2 coverage. We find that small changes in the density of CeO_2 nanocubes leads to dramatic enhancements in catalyst performance and that H_2 production rate varies non-monotonically as a function of CeO_2 coverage. Using in situ near-ambient pressure XPS (NAP-XPS) and ex situ high-angle annular dark-field scanning transmission electron microscopy (HAADF-STEM), we find that mesoscale domain boundaries between regions of densely packed CeO_2 nanocubes and bare Ni metal control formation of the Ni@CFIL active phase. These mesoscale boundaries give rise to a C gradient between regions of Ni metal characterized by heavy C deposition and CeO_2 domains characterized by hydroxyl formation and minimal C deposition. This C gradient is critical for nucleation of CFIL via a Ni@CFIL tip growth mechanism leading to stable H_2 generation, compared to typical coking leading to Ni encapsulation and rapid deactivation.(9, 17, 24, 25) The net result is that by carefully controlling the morphology of CeO_2 nanocubes on Ni, it is possible to template formation of the Ni@CFIL active phase in order to achieve stable H_2 production from ethanol.

EXPERIMENTAL

CeO_2 Nanoparticle Synthesis

To synthesize CeO_2 nanocubes, 15 mL of a 16.7 mM aqueous cerium (III) nitrate hexahydrate solution was prepared and transferred to a 50-mL, teflon-lined autoclave reactor. Following this, 15 mL of toluene was added along with 1.5 mL of oleic acid and 0.15 mL of tert-butyl amine. The autoclave reactor was then placed in an oven at 180 °C for 24 h.(26) After 24 h, the reaction mixture was removed, and the resulting crude was centrifuged at 3,000 rpm for 5 min. Following centrifugation, the upper organic layer was collected and precipitated with twice the volume in ethanol and centrifuged again at 8700 rpm for 15 minutes. The precipitated nanoparticles were dispersed in 5 mL of hexanes and washed with twice the volume in ethanol and centrifuged at 8700 rpm for 15 minutes two additional times. Finally, the nanoparticles were dispersed in 7 mL of chloroform in preparation for Langmuir-Blodgett deposition.

Langmuir-Blodgett Deposition

Langmuir-Blodgett (LB) deposition was performed using a NIMA 612D LB Trough system. 100 nm of Ni metal was thermally evaporated onto Si wafers containing a 500 nm thermal oxide layer. The resulting Ni film was subjected to UV treatment for 10 minutes to render the surface hydrophilic before LB deposition. The Ni sample was attached to a stepper motor and submerged vertically in the water-filled LB trough. CeO_2 nanocubes dispersed in chloroform were introduced using a 1 mL syringe to the surface of the trough. Approximately 500 μL of CeO_2 suspension was added such that the surface pressure of the trough was between 10–15 mN/m. The surface pressure of the trough was monitored with a Wilhelmy plate attached to a microbalance. The chloroform solvent was allowed to evaporate for 30 min after which teflon barriers at the ends of the trough start to compress. A surface pressure isotherm is automatically plotted during the compression allowing fine control of nanoparticle coverage. When a desired coverage is reached on the surface of the trough, the sample is pulled up at 2 mm/min resulting in the transfer of CeO_2 nanoparticles onto the Ni film. Prior to catalytic reactions the CeO_2-on-Ni catalysts were calcined on a hot plate at 500 °C followed by reduction in 250 Torr H_2 at 250 °C for 3 hours. As shown in the Figure S1 of the Supporting Information, calcination results in complete removal of the oleic acid capping agent from the deposited nanoparticles.

Ethanol Steam Reforming Kinetics

Kinetic measurements were carried out in a gas phase batch reactor equiped with a gas chromotograph (Agilent 7890B) for product quantification. A flame ionization detector was used to detect hydrocarbon products and a thermal conductivity detector with nitrogen as a reference flow was used to detect H_2. Acetaldehyde and ethanol were seperated on a Supelcowax capillary column, whereas a MoleSieve Ultimetal packed column was used to seperate CO_2, CO, CH_4, and H_2. A vial containing a 10% ethanol solution in water was attached to a gas-manifold, and the mixture underwent three freeze-pump cycles prior to introducing 10 Torr of ethanol/water vapor from the vial head-space into the reaction chamber. Pressure was monitored using a baratron capacitance gauge. The resulting gas-phase mixture corresponded to a 1:3 ratio of ethanol:water as quantified by gas chromatography. Following the introduction of the ethanol/water mixture, N_2 was introduced to bring the chamber to ambient pressure (760 Torr). A metal-bellows recirculation pump was used for gas-mixing and a boron-nitride substrate heater was used to control the catayst temperature. Unless otherwise noted, reactions were carried out at 360 °C, and product sampling was performed at 5 min intervals for 3 h. Area normalized rates were calculated by taking the peak area units for each product (H_2, CH_4, CO, and CO_2) and converting to units of mTorrs using detector sensitivity factors. The rates in mTorr/minutes were then normalized to the planar surface area of the catalyst (cm^2) to obtain the area normalized rates in units of mTorr min^{-1} cm^{-2}. Further calculations of H_2 turnover frequency normalized to Ni sites are provided in the Supporting Information Section 7 and calculations of selectivity for C-containing products are provided in the Supporting Information Section 8.

Transmission Electron Microscopy

To characterize nanoparticle coverage as a function of LB compression, CeO_2 nanocubes were deposited on carbon film TEM grids and imaged as deposited using a FEI Biotwin G2 Spirit electron microscope operating at 120 kV acceleration voltage. To image the Ni metal catalyst and CeO_2 nanoparticles following pre-treatment and catalytic reaction, Ni metal films and CeO_2 nanoparticles were deposited as described above onto Si_3N_4 TEM grids (50 nm thickness) and analyzed by HAADF-STEM imaging and X-ray energy-dispersive spectroscopy (EDS) using an FEI Titan G2 60-300 S/TEM microscope operating at 300 kV acceleration

voltage. HAADF-STEM images were collected with a convergence angle of 10 mrad and collection angles of 106–200 mrad to enhance atomic (Z) contrast.

X-Ray Photoelectron Spectroscopy

Catalysts were characterized using both ex situ (ultrahigh vacuum) and in situ (near ambient pressure) measurements. Ex situ XPS measurements were carried out using a Kratos Ultra-Axis XPS system with an Al kα source operating at 120 W with a 12 kV accelerating voltage. Survey spectra were collected at 100 eV pass energy and high-resolution spectra were collected at 20 eV pass energy. In situ measurements were carried out using a SPECS NAP-XPS system in the Surface Analysis Facility at Ohio State University. The system is equipped with a NAP-reaction cell where 0.75 Torr of a 1:3 ethanol:water mixture was introduced via a vial on the instrument manifold following freeze pump cycles. As needed H_2 and O_2 gasses were also introduced to the NAP-reaction cell via mass flow controllers. Fits to all spectra were performed using CASA-XPS software, and peak areas of each element were normalized using the relative sensitivity factors.

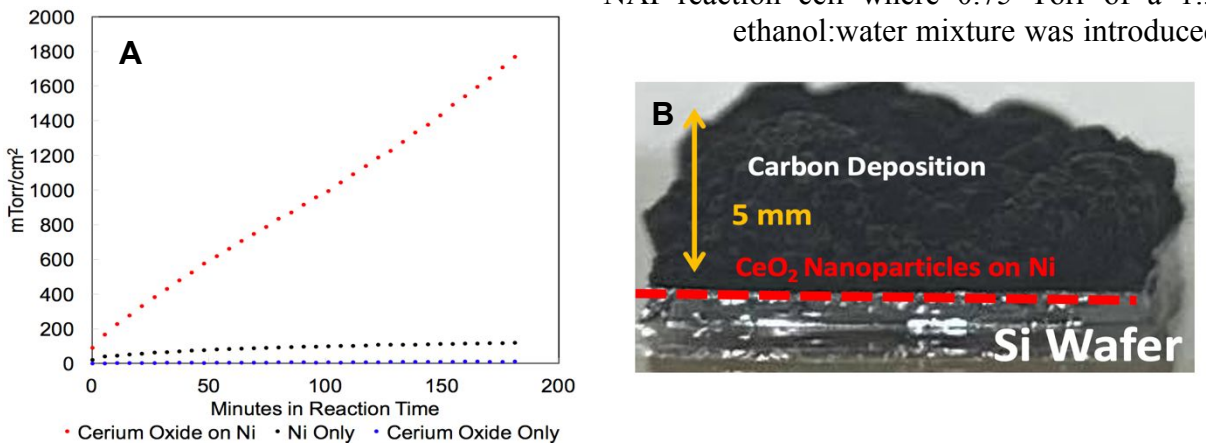

Figure 1. (A) H_2 production rate as a function of time observed on the Ni/CeO_2 catalyst (red), pure Ni catalyst (black), and pure CeO_2 catalyst (blue) in 10 Torr of a 1:3 ethanol:water mixture at 360 °C. **(B)** Carbon deposition visually observed on Ni/CeO_{22} catalyst post-reaction.

RESULTS AND DISCUSSION

Deactivation-Free H_2 Production by Ni@CFILs

CeO_2 nanocubes were deposited on Ni thin films using Langmuir Blodgett (LB) deposition to fabricate an inverse catalyst. In related previous studies we have shown that using this technique, the coverage of discrete CeO_2 nanocubes on metal thin films can be controlled from the monolayer to submonolayer levels.(27, 28) Catalytic rates for production of H_2 gas were measured for 1) pure Ni films without CeO_2, 2) pure CeO_2 nanocubes without Ni, and 3) CeO_2 nanocubes deposited on Ni films. Figure 1A shows the production of H_2 as a function of time during a 3 h reaction for these three catalysts.

Pure CeO_2 shows almost no H_2 production indicating that CeO_2 alone is not active for ESR. In contrast pure Ni catalysts shows mild activity towards H_2 gas production but results in rapid deactivation within the first 30 min of catalytic testing. Only in the case of Ni/CeO_2 is the activity towards H_2 gas sustained, and no sign of deactivation is observed for the course of a 3 h

reaction. The rate of H_2 production on the Ni/CeO_2 catalyst is greater than 10-fold more active compared to pure Ni. Oxidation of C deposits on Ni by the CeO_2 co-catalyst is one mechanism of enhancing activity and preventing deactivation. However, inspection of the Ni/CeO_2 catalyst post-reaction reveals the formation of CFILs that accumulate to a height of over 5 mm on the planar surface as shown in the photograph in Figure 1B.

Various mechanisms exist for C deposition, and some of these lead to rapid deactivation by site blocking while others do not necessarily result in catalyst deactivation.(9, 17, 24) For example, Xu et. al reports TEM characterization of Ni supported on CeO_2 showing that under certain conditions formation of porous CFIL is favored as opposed to encapsulating surface C.(24) The difference in these two C deposition mechanisms is that while formation of CFIL allows continued access of reactant gasses to the catalyst surface, encapsulating C grows over metal active sites resulting in catalyst deactivation.(24) CFIL growth on thin films have been widely studied on supported metal nanoparticles and thin film catalysts. The mechanism of CFIL growth can be divided into either a tip-growth mechanism or a base growth mechanism.(29-33) Figure 2A and B graphically depicts these two growth mechanisms. In a tip-growth mechanism, the catalyst for CFIL formation resides at the tip of a CFIL and moves upward with the filament during growth. In contrast, during a base growth mechanism, the catalyst resides at the base of the CFIL while the filament is pushed upward during growth. For this reason, the base growth mechanism is more prone to deactivation by encapsulation of the catalyst.(19, 24)

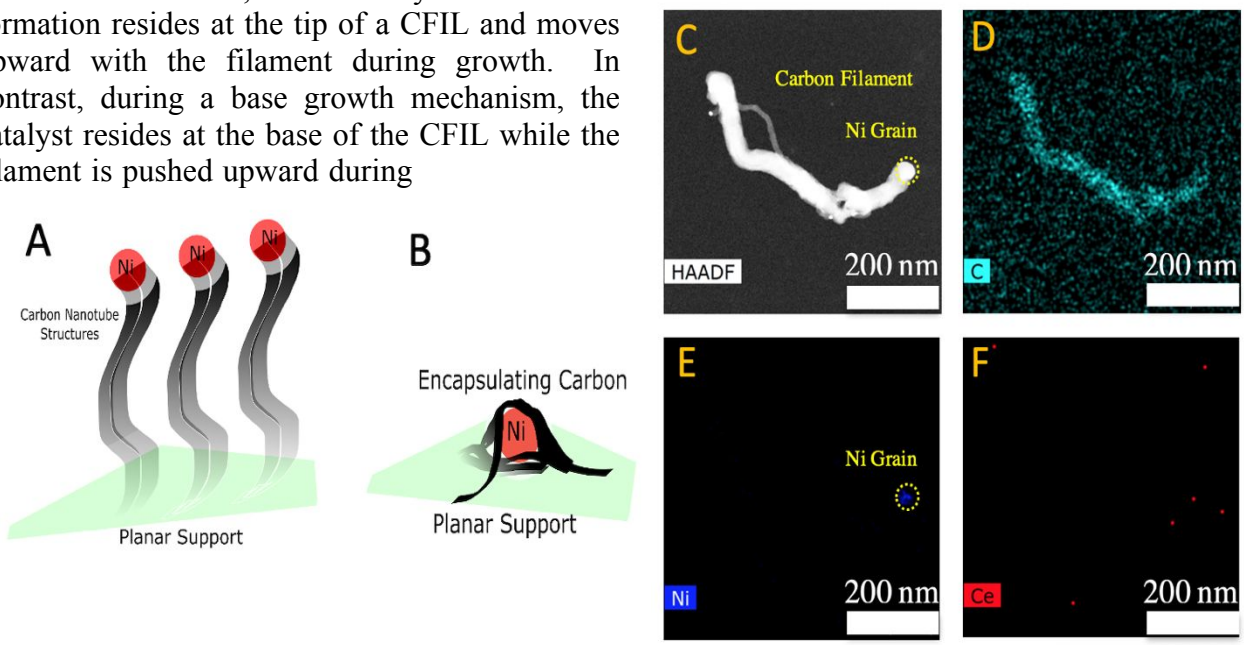

Figure 2. **(A)** Two mechanisms of C deposition on a Ni catalyst: **(A)** shows tip growth where C precipitation pushes Ni upward leading to the formation of Ni-tipped CFILs. B shows base growth where uniform deposition of C across a Ni surface leads to Ni encapsulation and catalyst deactivation. **(C)** HAADF TEM images of post-reaction Ni@CFIL catalyst. **(D)** EDAX analysis for C on the filament structure. **(E,F)** EDAX analysis of the HAADF-STEM image shown in C. E shows Ni at the tip of the CFIL, and F confirms the absence of CeO_2 anywhere along the CFIL.

To understand the mechanism of C deposition on the active Ni/CeO_2 catalyst studied here, HAADF-STEM imaging with energy dispersive x-ray analysis (EDAX) was carried out on samples obtained from the catalyst surface following ESR. Figure 2C shows a representative HAADF-STEM image while D-F show the EDAX mapping of C, Ni, and Ce, respectively. These images show that the deposition of surface C occurs in the form of CFILs. EDAX mapping confirms the presence of Ni near the tip of the CFIL, whereas Ce content along the filament is undetectable within the bremsstrahlung baseline (2E and 2F). This characterization confirms that on the active Ni/CeO_2 catalyst, C deposition occurs primarily through the growth of CFILs via a tip-growth mechanism.

Dynamic Stability of Ni@CFIL Active Phase

To understand the nature of the Ni@CFIL active catalyst, NAP-XPS was utilized to probe the catalyst under in situ reaction conditions. We note that while the STEM images discussed above represent spatially resolved characterization of the active phase, the NAP-XPS measurements presented below represent a spatially averaged result over a large area of the catalyst surface. However, as described below, we find good correlation between these characterization methods. In these experiments ESR was first carried out on a Ni/CeO_2 catalyst inside a batch reactor filled with 10 Torr of 1:3 ethanol:water mixture at 360 °C for 3 h to allow the Ni@CFIL active phase to form and reach a steady state. This ex situ pre-treatment was necessary for NAP-XPS analysis of the Ni@CFIL active phase because CFIL growth rate is much lower under the reduced pressure (<1 Torr) attainable in the NAP-XPS reaction cell. Following ex situ growth of the Ni@CFILs active phase, this same catalyst was then removed from the batch reactor and immediately loaded into the NAP-XPS instrument. XPS spectra were then collected first under UHV at room temperature and then in 0.75 Torr of a 1:3 ethanol:water mixture at 280 °C and 360 °C. Following this sequence, the catalyst was cycled between UHV at room temperature and 0.75 Torr ethanol/water at 360 °C to determine reversible changes to the catalyst under reaction conditions. The results of this experiment for Ni 2p and Ce 3d spectra are summarized in Figure 3, and corresponding C and O spectra are shown in Figure S2 of the Supporting Information. Under UHV the surface of the catalyst consists of predominantly

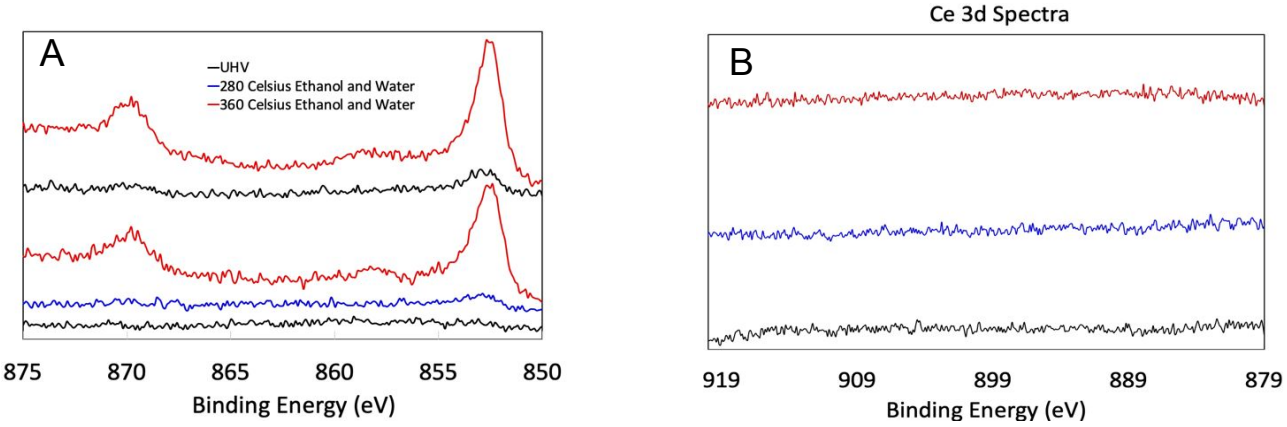

Figure 3. In situ NAP-XPS measurements of the Ni 2p spectrum **(A)** and the Ce 3d spectrum **(B)** on Ni/CeO_2. Spectra are obtained in 0.75 Torr of a 1:3 ethanol:water mixture at 280 °C (blue spectra) and 360 °C (red spectra) following the ex situ formation of the Ni@CFIL active phase. For reference spectra of the Ni@CFIL active phase under UHV at room temperature is shown in black. These spectra show that Ni metal reversibly emerges from the network of CFILs when the catalyst temperature is elevated to 360 °C during reaction, but CeO_2 is absent from the active phase under all conditions tested.

graphitic carbon and shows only trace amounts of Ni and no detectable Ce. Addition of 0.75 Torr ethanol/water and heating to 280 °C resulted in no significant changes. However, when the temperature was raised to 360 °C, a clear Ni 2p spectrum is observed. Pumping out the ethanol/water mixture and returning the catalyst to room temperature, resulted in nearly complete loss of the Ni 2p signal, while returning the catalyst to reaction conditions restored the Ni 2p signal, indicating that the emergence of Ni under reaction conditions is reversible. Determining the oxidation state of the Ni active phase during reaction conditions can be challenging although in in-situ XPS spectra here indicate that the binding energy of nickel has a prominent peak centered around 852.5-852.6 eV which indicates it is mainly in the metallic state, consistent with in-situ XRD studies conducted by Liu et al.(19, 34)

This observation is consistent with a number of environmental TEM studies, which show that metal grains dynamically move in and out of carbon filament structures depending on temperature and pressure conditions, and this effect is the result of reversible transition between Ni metal and NiC_x carbide phases.(29-32, 35-38) During ESR the growth of CFILs is a dynamic process where the Ni catalyst is continuously pushed upward at or near the tip of a CFIL allowing Ni to remain accessible to reactant gases, thereby preventing deactivation. During ESR the Ni grain at the tip of the CFIL remains active for H_2 production as has also been recently observed by Xu et al.(24) The absence of Ni 2p XPS signal at temperatures below 280 °C is likely due to dissolution of Ni into C via the formation of NiC_x carbide phases, which are thermodynamically favorable at temperatures below 280 °C as reported by Liu et al.(23) We hypothesize that the reason we do not observe NiC_x at these temperatures is that the very small Ni:C ratio yields the Ni catalyst undetectable upon dissolution into the much more abundant C background. Formation of NiC_x would result in diffusion of Ni into CFILs due to the high solubility of Ni in C at temperatures below 280 °C. We hypothesize that this diffusion of soluble Ni into the CFILs places Ni beyond the probe depth of the XPS measurement, which could explain why we cannot observe the NiC_x in these measurements. Decomposition of the NiC_x pase has previously been shown to occur between 280 and 360 °C.(23) This leads to Ni precipitation in the form of metallic nanoparticles at the tips of CFILs as observed here by NAP-XPS, allowing for continued CFIL growth and H_2 production via the tip growth mechanism. This dissolution and re-precipitation of Ni metal is reversible during repeated temperature cycling as shown here. Note that these measurements do not distinguish whether the reversible appearance of Ni under reaction conditions is due entirely to temperature cycling or if the gas environment also plays a role. Here we simply confirm that Ni reversibly emerges for the CFIL matrix under reaction conditions, which explains the resistance of this catalyst to deactivation by C deposition, and future studies will be needed to fully understand the driving force responsible for this effect. It is also not possible to entirely rule out that the reversible appearance of Ni is partly due to C removal by active surface O species during reaction. However, this explanation is not completely consistent with the kinetic results showing that the highest H_2 activity occurs on catalysts that also show the greatest amount of C deposition (see Figure 1) as well as STEM imaging showing that CeO_2 is absent from the Ni@CFIL active phase (see Figure 2). For these reasons, we believe that the previous hypothesis of Ni solubility in C is most probable, although partial C removal by surface hydroxyls under reaction conditions may also contribute to a lesser extent.

Consistent with EDAX mapping of the Ni@CFIL catalyst (Figure 2), Figure 3B shows that no Ce is detected by NAP-XPS under any temperature or pressure conditions investigated here. These results indicate that unlike Ni, CeO_2 remains at the base of the catalyst during growth of the CFILs and is absent from the Ni@CFIL active phase. It has been established in previously reported ESR catalysts that CeO_2 plays an important role in C removal by catalyzing H_2O

dissociation. We believe that in the catalysts studied here CeO_2 likewise serves to dissociate H_2O during the initial stages of reaction, leading to a C gradient near the Ni/CeO_2 interface. This C gradient is key to templating the formation of the Ni@CFIL active phase as described below. To confirm that the loss of Ce signal shown in Figure 3B is the result of CeO_2 encapsulation, the Ni 2p and Ce 3d XPS spectra of the pre-reaction catalyst were also measured. These spectra, which show a clear Ce signal, are provided as Figure S3 of the Supporting information.

Ni/CeO_2 Interface Templates Formation of Ni@CFILs

To investigate the respective roles of Ni and CeO_2 in enhancing catalytic activity relative to either Ni or CeO_2 alone, NAP-XPS measurements were performed on pure Ni films and pure CeO_2 nanocubes deposited directly on SiO_2. In contrast to Figure 3, this data was obtained on fresh catalysts following calcination at 500 °C and reduction in H_2 at 250 °C, but before ESR reaction, so no C was pre-deposited on the surface. Accordingly, initial spectra of these samples obtained in UHV show almost no surface C present indicating that catalyst pre-treatment completely remove the oleic acid capping agent from the as-synthesized CeO_2 nanocubes while leaving the CeO_2 morphology relatively unchanged (see Supporting Information sections 1 and 2). To understand C deposition under ESR-like reaction conditions, Figure 4A shows the C 1s spectra on pure Ni and pure CeO_2 at 360 °C in 0.75 Torr of pure ethanol. Comparing these two spectra reveals that C deposition occurs efficiently on Ni surfaces due to its ability to break C-C and C-H bonds, while relatively little C deposition occurs on CeO_2 without Ni.

Similar NAP-XPS measurements were also performed on Ni/CeO_2 catalysts as a function of CeO_2 coverage. The C:Ni ratio measured at 360 °C in a 0.75 Torr 1:3 ethanol:water mixture is plotted in Figure 4B. These results show that the higher the CeO_2 coverage, the lower the C deposition under reaction conditions. This observation is consistent with previous findings that during ESR, CeO_2 promotes C removal via dissociation of H_2O and the spillover of surface hydroxyls from CeO_2 to Ni.(19, 23) Based on this we hypothesize that CeO_2 plays a role in nucleation of the Ni-tipped CFILs active phase by promoting formation of a surface C gradient as is required for a CFIL tip-growth mechanism. Specifically, a C gradient will form at the interface between Ni and CeO_2, where Ni covered by CeO_2-rich domains will accumulate less C compared to Ni metal regions containing a low surface coverage of CeO_2 nanocubes.

In previous work, Gili et al. showed that following hydrocarbon decomposition on a Ni catalyst, three unique cubic NiC_x carbide phases formed from C interstitially dissolved in the Ni metal lattice.(35) Upon saturation of the phase with the highest C content, graphitic C precipitates. If C is uniformly dissolved in Ni, then precipitation occurs evenly across the

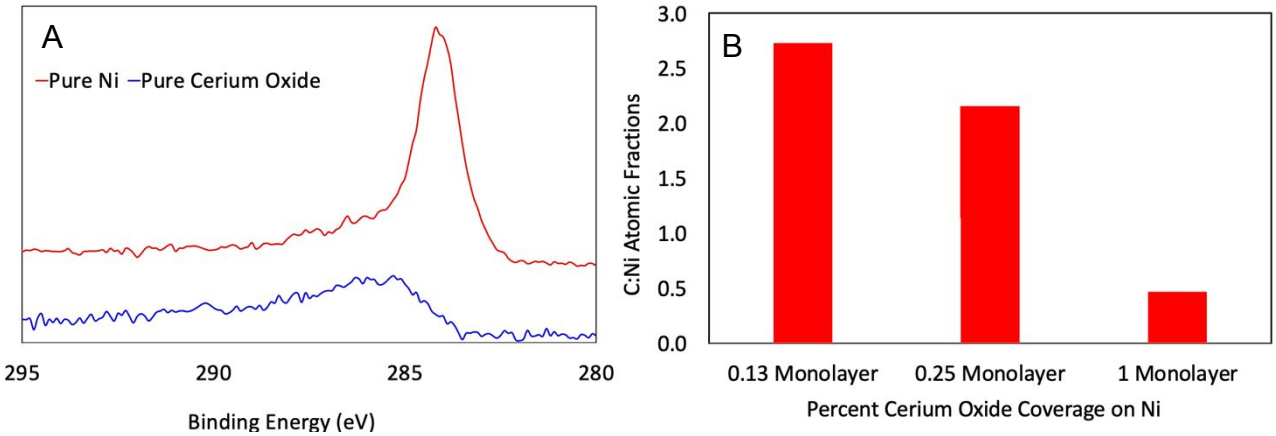

Figure 4. **(A)** NAP-XPS measurements of C 1s spectra at 360 °C under 0.75 Torr of ethanol (no water) on a pure Ni catalyst (red) and a pure CeO_2 catalyst (blue). This comparison confirms that C preferentially deposits on Ni rather than on CeO_2. **(B)** C:Ni atomic fraction measured by NAP-XPS during reaction as a function of increasing CeO_2 nanocube coverage on Ni. Spectra are obtained at 360 °C under 0.75 Torr of a 1:3 ethanol:water mixture. Results show decreasing C deposition on Ni catalysts with increasing CeO_2 coverage.

surface leading to C encapsulation and catalyst deactivation. However, if C deposition is not uniform but instead occurs along a gradient, then the directional precipitation of graphitic C will propel Ni nanoparticles away from the surface resulting in CFIL formation by a tip growth mechanism. Consequently, the ability to template the non-uniform deposition of C on a Ni surface is critical to initiation the tip-growth mechanism. This mechanism is further reinforced in work by Xu et. al where a C gradient was also proposed to result in C precipitation to CFIL formation by a tip-growth mechanism under water rich conditions for ESR.(24)

Effects of Nano and Meso-Scale CeO_2 Morphology

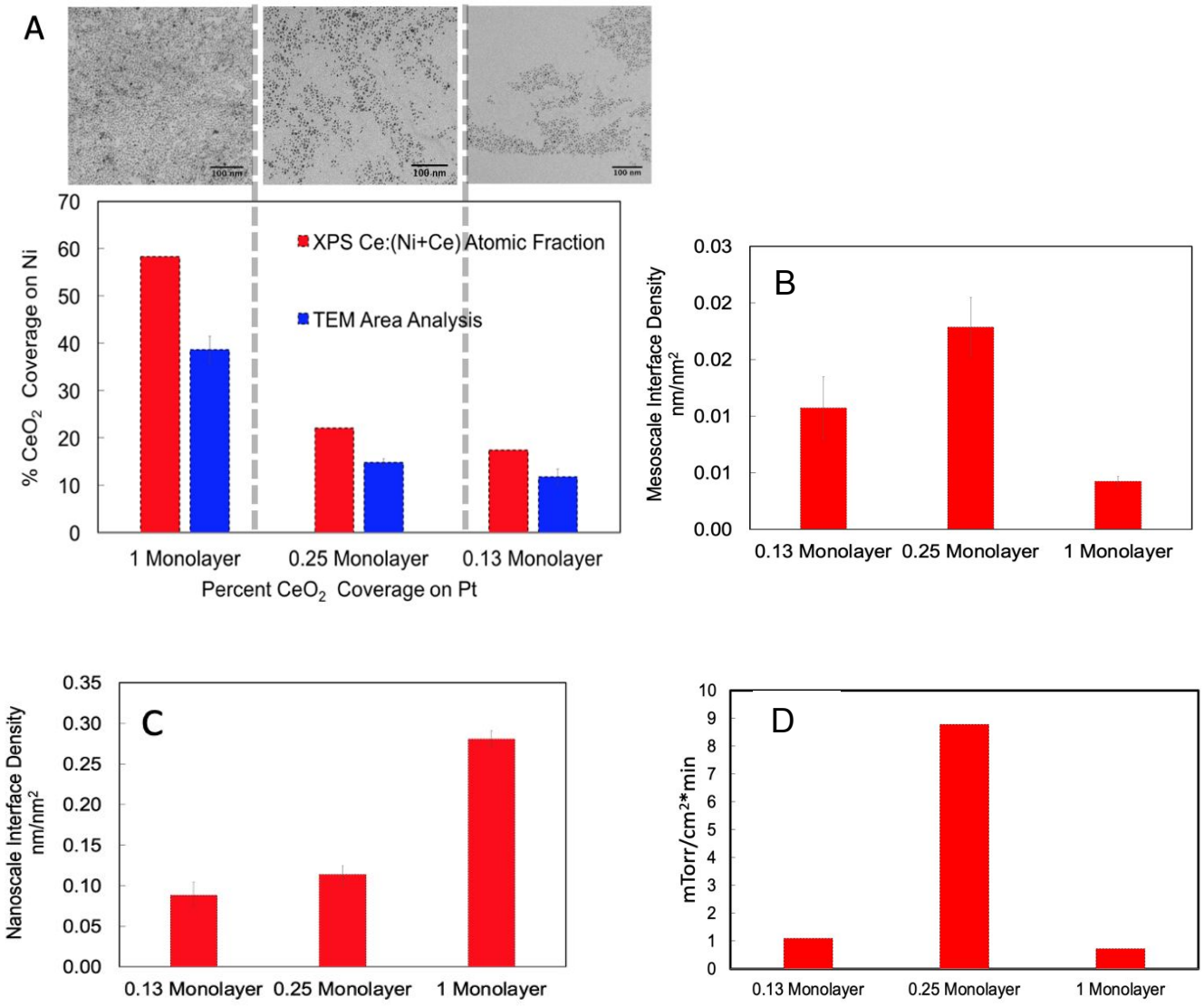

Figure 5. (A) Coverage of CeO_2 nanocubes deposited on Ni as a function of LB compression. Coverage is quantified by two methods: Ce:(Ce+Ni) atomic fraction measured by XPS (red) and TEM area analysis (blue). Insets show TEM images of each sample consisting of CeO_2 nanocubes deposited at 1.0, 0.25, and 0.13 monolayer coverage, respectively. **(B)** Mesoscale interface density and **(C)** nanoscale interface density as a function of CeO_2 nanocube surface coverage measured by TEM image analysis. **(D)** H_2 production rates during ESR measured on Ni/CeO_2 as a function of CeO_2 nanocube surface coverage showing that activity closely correlates with the mesoscale, rather than nanoscale interface. These results indicate that CeO_2 morphology controls activity by templating the formation of a Ni@CFIL active phase through creation of a surface C gradient.

To understand the formation of C gradients that template the Ni@CFIL active phase, Figure 5A shows a TEM images of CeO_2 nanocubes deposited by LB deposition. Depending on the surface concentration of CeO_2 on the underlying Ni, the CeO_2 nanocubes can self-assemble forming two different types of morphologies. We find that CeO_2 nanocubes deposit as uniform regions of densely packed particles interspersed with void regions representing a bare Ni metal catalyst. To describe this morphology, we define a nanoscale interface as the 3-phase boundary representing the perimeter of an individual CeO_2 nanocube on Ni, which is in contrast to a mesoscale interface, which we define as the boundary between a region of densely packed CeO_2 nanocubes and clean Ni metal. Based on the NAP-XPS data shown in Figure 4B, we expect a C gradient will form across the mesoscale domain boundaries where less C will be present in the regions of high CeO_2 coverage, and comparatively greater C deposition will occur on the bare Ni metal outside the reach of surface hydroxyls, which form primarily on CeO_2.(39, 40) This mechanism can be as a carbon gradient which forms away from densely packed CeO_2 domains, this is followed by the growth of carbon filaments on Ni sites. Xu et. al have ascribed the formation of a carbon gradient on Ni grains to be the premise for tip-growth of filaments where the tip of the grain was hypothesized to be kept clean by water while carbon accumulates and precipitates from the other end of the grain.[21]

Assuming this mechanism where CeO_2 templates the formation of the Ni@CFIL active phase, we expect catalyst activity to show a strong dependence on CeO_2 coverage. To investigate this effect, films of CeO_2 nanocubes were deposited at 1.0 monolayer, 0.25 monolayer, and 0.13 monolayer on Ni thin films using LB deposition. Here samples designated as 1.0 monolayer CeO_2 corresponds to the LB compression required to achieve saturation of the surface pressure resulting from close packing of the CeO_2 nanocubes. Sub-monolayer samples were prepared by scaling the LB compression area to achieve the desired sub-monolayer coverage. Figure 5A show XPS and TEM quantification of CeO_2 coverage for these three samples, and the above inset show the corresponding TEM images for each surface coverage on Ni. XPS quantification in Figure 6A (red) shows an increase in the Ce:Ni atomic fraction as the coverage of CeO_2 nanocubes was increased from 0.13 to 1.0 monolayer. Coverage quantification by TEM area analysis in (blue) confirms the trend observed from XPS. The slight discrepancy observed between XPS and TEM quantification methods can be attributed to photoelectron signal detected throughout the entire cross-section of 5 nm CeO_2 nanocubes during XPS analysis resulting in a higher Ce:Ni atomic ratio relative to planar quantification from TEM analyses.

To quantify how density of nano and mesoscale interfaces influences catalytic performance, TEM image analysis was carried out (Figure 5B-C) and compared with H_2 production rates as shown in Figure 5D. The density of nanoscale phase boundaries is expected to scale directly with CeO_2 nanocube packing density on Ni. In contrast, the density of mesoscale domain boundaries depends non-monotonically on the packing morphology of the CeO_2 layer as shown in the three TEM images in Figure 5A. Using TEM image analysis, we quantified both nano and mesoscale interface densities in units of lineal distance per area (nm/nm^2) as a function of total CeO_2 coverage. Analysis is performed across multiple regions of a given sample, and results are averaged to yield data sets with statistical significance (standard deviation). Details of this analysis are provided in the Supporting Information Figure S4. Results show that the nanoscale interface density increases monotonically with CeO_2 nanocube coverage as expected (Figure 5B). In contrast, the mesoscale interface density shows a

maximum at a CeO_2 nanocube coverage of 0.25 monolayer (Figure 5C). At 0.13 monolayer coverage, the density of mesoscale boundaries decreases due to a fewer domains of densely packed CeO_2 nanocubes, while at 1.0 monolayer the density of mesoscale boundaries decrease due to coalescence of multiple close-packed domains leading to a uniform coverage of closely spaced CeO_2 nanocubes with few regions of clean Ni remaining. To confirm that the density of interface sites does not change during reaciton due to particle sintering, we have performed TEM imaging of CeO_2 nanocubes deposited on Si_3N_4 membranes before and after reaction. These images are shown in Figure S5 of the Supporting Information and confirm that the CeO_2 nanocubes are thermally stable and do not sinter during reaction.

Figure 5D shows H_2 production rates for Ni/CeO_2 catalysts as a function of CeO_2 coverage and corresponding deactivation profiles are shown in Figure S6 of the Supporting Information. We find that H_2 production was enhanced by almost one order of magnitude for Ni sample containing 0.25 monolayer of CeO_2 nanocubes compared to either a higher or lower CeO_2 coverage.(24, 35) By comparison, addition of CeO_2 to Ni at either 0.13 monolayer or 1.0 monolayer coverages showed only small enhancements in H_2 production compared to pure Ni. We note that the most active sample does not correspond to the highest density of nanoscale Ni/CeO_2 interface sites, but rather represents the highest density of mesoscale boundaries between domains of densely packed CeO_2 nanocubes and regions of clean Ni.

This correlation is consistent with results above indicating that CeO_2 is not directly involved in the catalytic reaction but rather serves to template the formation of Ni@CFIL active sites via a CFIL tip-growth mechanism. HAADF-STEM imaging with EDAX analysis (Figure 2) as well as NAP-XPS measurements (Figure 3) confirm that CeO_2 is not present at or near the Ni@CFIL active sites. Rather NAP-XPS measurements indicate that C gradients can form at the interface between clean Ni and CeO_2-rich domains on the catalyst surface (Figure 4). As previously reported, this gradient of C deposits is critical to facilitate CFIL formation via a tip growth mechanism.(24, 35) Figure 6 graphically portrays the process for which the mesoscale interface of CeO_2 domains induces a carbon gradient on neighboring Ni regions which results in the growth of carbon filament on Ni grain.

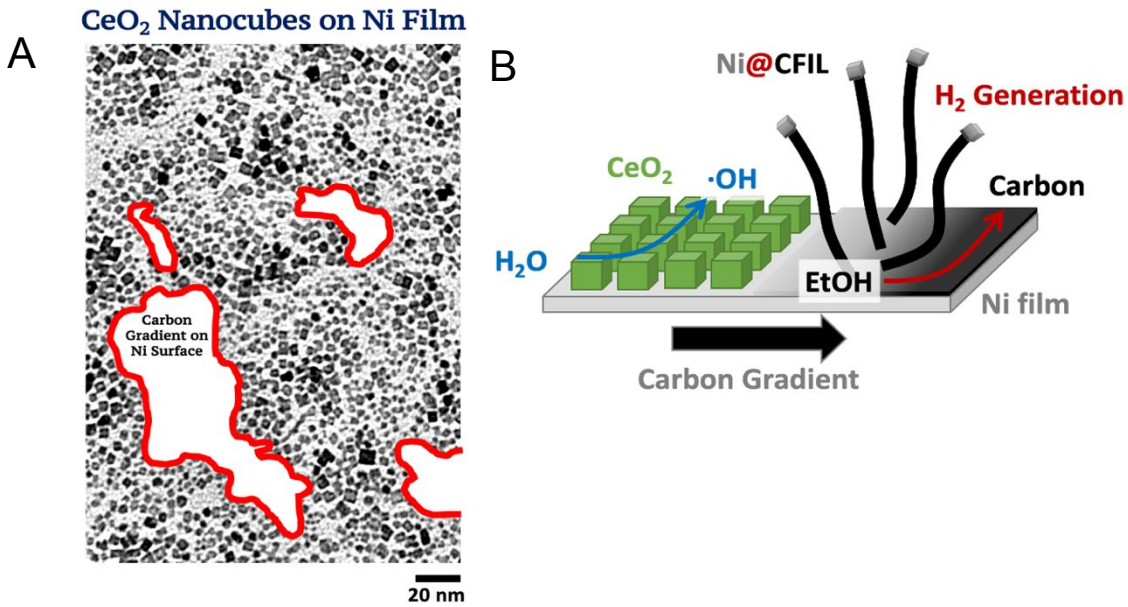

Figure 6 (A) TEM micrograph depicting mesoscale domains of CeO2 nanoparticles and exposed Ni domains. **(B)** Mechanistic depiction of the mechanism for which the mesoscale interface of CeO_2 nanocubes templates the formation of carbon filaments at neighboring Ni grain.

Zhang et al. has reported a turnover frequency (TOF) of approximately 8×10^{-3} s^{-1} for ethanol conversion during ESR on Ni nanoparticles in a Ni/CeO_2 impregnated catalyst system at 350 °C.(41) On Fe-Rh bimetallic catalysts, TOF for ESR is reported to be as high as 0.3 s^{-1} at 370 °C.(20) To compare the ESR activity reported here to these prior studies, we calculate that the area normalized rate for H_2 production on the Ni/CeO_2 catalyst containing a 0.25 monolayer CeO_2 coverage represents a TOF of 0.2 s^{-1} (see Section 7 of the Supplementary Information). Because it is not possible to directly measure the Ni dispersion in these planar catalysts, this calculated TOF assumes a Ni site density of 1.86×10^{15} cm^{-2} based on a clean Ni (111) surface prior to deposition of CeO_2 nanocubes. In reality, this represents a conservative estimate to the TOF because only a small fraction of the total Ni surface area in the as-prepared catalyst is actually incorporated into the Ni@CFIL active phase based on the mesoscale packing of CeO_2 nanocubes (see Figures 2 and 3). Although this value almost certainly underestimates the true TOF of the Ni@CFIL active phase, it serves as a useful comparison showing that the activity of these Ni-based model systems is quite high compared to previously reported Ni catalysts while still maintaining strong resistance to deactivation. While both activity and resistance to deactivation are high, this catalyst shows low selectivity for CO_2, producing CO, methane, and acetaldehyde as the primary C-containing products (see Figure S7 of the Supplementary Information). CeO_2 is known to promote the water gas shift reaction as well as methane reforming leading to CO_2.(42-45) However, consistent with the absence of CeO_2 from the Ni@CFIL active phase, only trace amounts of CO_2 are observed from these catalysts.

CONCLUSIONS

In summary, we find that catalysts prepared by carefully controlled deposition of CeO_2 nanocubes on Ni metal films show high activity for ESR, enhancing the rate of H_2 production by more than a factor of 10 compared to pure Ni. Contrary to the idea that a catalyst should be kept free from C deposition to prevent deactivation, we find that the most active Ni/CeO_2 catalysts experience significant C deposition during ESR but show no deactivation. HAADF-STEM imaging shows that the catalyst active phase is Ni@CFIL, which forms during reaction via a CFIL tip-growth mechanism. In situ NAP-XPS shows that Ni catalysts at the tips of CFILs remain accessible under reaction conditions leading to the continuous production of H_2 with no deactivation resulting from C deposition. Interestingly, no CeO_2 is observed at or near the Ni@CFIL active phase either ex situ by EDAX mapping or in situ by NAP-XPS. Instead we find that the role of CeO_2 is to template the formation of the Ni@CFIL active phase by producing a C gradient at the Ni/CeO_2 interface, which has been shown to be necessary to achieve Ni tip-mediated CFIL growth. These findings indicate that in addition to the chemical composition of Ni/CeO_2 bifunctional catalysts, the mesoscale morphology of the interface is a critical parameter for predicting activity, and if well-controlled, this morphology can be used to template the formation of a Ni@CFIL active phase that resists traditional deactivation via a CFIL tip-growth mechanism.

AUTHOR INFORMATION

Corresponding Author

* Email: baker.2364@osu.edu

ACKNOWLEDGEMENTS

Ambient pressure XPS was supported by the National Science Foundation through NSF award 1625792. Electron microscopy was performed at the Center for Electron Microscopy and Analysis (CEMAS) at The Ohio State University.

REFERENCES

1. Vaidya PD, Rodrigues AE. Insight into steam reforming of ethanol to produce hydrogen for fuel cells. Chemical Engineering Journal. 2006;117(1):39-49.
2. Liguras DK, Kondarides DI, Verykios XE. Production of hydrogen for fuel cells by steam reforming of ethanol over supported noble metal catalysts. Applied Catalysis B: Environmental. 2003;43(4):345-54.
3. Rabenstein G, Hacker V. Hydrogen for fuel cells from ethanol by steam-reforming, partial-oxidation and combined auto-thermal reforming: A thermodynamic analysis. Journal of Power Sources. 2008;185(2):1293-304.
4. Frusteri F, Freni S, Chiodo V, Spadaro L, Di Blasi O, Bonura G, et al. Steam reforming of bio-ethanol on alkali-doped Ni/MgO catalysts: hydrogen production for MC fuel cell. Applied Catalysis A: General. 2004;270(1-2):1-7.
5. Koh AC, Leong WK, Chen L, Ang TP, Lin J, Johnson BF, et al. Highly efficient ruthenium and ruthenium–platinum cluster-derived nanocatalysts for hydrogen production via ethanol steam reforming. Catalysis Communications. 2008;9(1):170-5.
6. Sanchez-Sanchez MC, Navarro Yerga RM, Kondarides DI, Verykios XE, Fierro JLG. Mechanistic aspects of the ethanol steam reforming reaction for hydrogen production on Pt, Ni, and PtNi catalysts supported on γ-Al2O3. The Journal of Physical Chemistry A. 2010;114(11):3873-82.
7. Kourtelesis M, Panagiotopoulou P, Verykios X. Influence of structural parameters on the reaction of low temperature ethanol steam reforming over Pt/Al2O3 catalysts. Catalysis Today. 2015;258:247-55.
8. Goula MA, Kontou SK, Tsiakaras PE. Hydrogen production by ethanol steam reforming over a commercial Pd/γ-Al2O3 catalyst. Applied Catalysis B: Environmental. 2004;49(2):135-44.
9. Montero C, Remiro A, Valle B, Oar-Arteta L, Bilbao J, Gayubo AG. Origin and nature of coke in ethanol steam reforming and its role in deactivation of Ni/La2O3–αAl2O3 catalyst. Industrial & Engineering Chemistry Research. 2019;58(32):14736-51.
10. Mathure PV, Ganguly S, Patwardhan AV, Saha RK. Steam reforming of ethanol using a commercial nickel-based catalyst. Industrial & engineering chemistry research. 2007;46(25):8471-9.
11. Haryanto A, Fernando S, Murali N, Adhikari S. Current status of hydrogen production techniques by steam reforming of ethanol: a review. Energy & Fuels. 2005;19(5):2098-106.
12. Sohn H, Soykal II, Zhang S, Shan J, Tao F, Miller JT, et al. Effect of cobalt on reduction characteristics of ceria under ethanol steam reforming conditions: AP-XPS and XANES studies. The Journal of Physical Chemistry C. 2016;120(27):14631-42.
13. Song H, Ozkan US. Changing the oxygen mobility in Co/Ceria catalysts by Ca incorporation: implications for ethanol steam reforming. The Journal of Physical Chemistry A. 2010;114(11):3796-801.
14. Wang F, Zhang L, Deng J, Zhang J, Han B, Wang Y, et al. Embedded Ni catalysts in Ni-O-Ce solid solution for stable hydrogen production from ethanol steam reforming reaction. Fuel Processing Technology. 2019;193:94-101.

15. Wang F, Zhang L, Zhu J, Han B, Zhao L, Yu H, et al. Study on different CeO2 structure stability during ethanol steam reforming reaction over Ir/CeO2 nanocatalysts. Applied Catalysis A: General. 2018;564:226-33.
16. Soykal II, Sohn H, Singh D, Miller JT, Ozkan US. Reduction characteristics of ceria under ethanol steam reforming conditions: effect of the particle size. ACS Catalysis. 2014;4(2):585-92.
17. Vicente J, Ereña J, Montero C, Azkoiti MJ, Bilbao J, Gayubo AG. Reaction pathway for ethanol steam reforming on a Ni/SiO2 catalyst including coke formation. International journal of hydrogen energy. 2014;39(33):18820-34.
18. Zhang C, Zhu W, Li S, Wu G, Ma X, Wang X, et al. Sintering-resistant Ni-based reforming catalysts obtained via the nanoconfinement effect. Chemical Communications. 2013;49(82):9383-5.
19. Liu Z, Duchoň Ts, Wang H, Peterson EW, Zhou Y, Luo S, et al. Mechanistic insights of ethanol steam reforming over Ni–CeO x (111): The importance of hydroxyl groups for suppressing coke formation. The Journal of Physical Chemistry C. 2015;119(32):18248-56.
20. Choong C, Zhong Z, Huang L, Borgna A, Hong L, Chen L, et al. Infrared evidence of a formate-intermediate mechanism over Ca-modified supports in low-temperature ethanol steam reforming. ACS Catalysis. 2014;4(7):2359-63.
21. Choong CK, Chen L, Du Y, Schreyer M, Ong SD, Poh CK, et al. The role of metal–support interaction for CO-free hydrogen from low temperature ethanol steam reforming on Rh–Fe catalysts. Physical Chemistry Chemical Physics. 2017;19(6):4199-207.
22. Sun J, Qiu X-P, Wu F, Zhu W-T. H2 from steam reforming of ethanol at low temperature over Ni/Y2O3, Ni/La2O3 and Ni/Al2O3 catalysts for fuel-cell application. International Journal of Hydrogen Energy. 2005;30(4):437-45.
23. Liu Z, Duchoň T, Wang H, Grinter DC, Waluyo I, Zhou J, et al. Ambient pressure XPS and IRRAS investigation of ethanol steam reforming on Ni–CeO 2 (111) catalysts: an in situ study of C–C and O–H bond scission. Physical Chemistry Chemical Physics. 2016;18(25):16621-8.
24. Xu W, Liu Z, Johnston-Peck AC, Senanayake SD, Zhou G, Stacchiola D, et al. Steam reforming of ethanol on Ni/CeO2: reaction pathway and interaction between Ni and the CeO2 support. ACS Catalysis. 2013;3(5):975-84.
25. Alberton AL, Souza MM, Schmal M. Carbon formation and its influence on ethanol steam reforming over Ni/Al2O3 catalysts. Catalysis Today. 2007;123(1-4):257-64.
26. Yang S, Gao L. Controlled synthesis and self-assembly of CeO2 nanocubes. Journal of the American Chemical Society. 2006;128(29):9330-1.
27. Yang X, Mueanngern Y, Baker QA, Baker LR. Crotonaldehyde hydrogenation on platinum–titanium oxide and platinum–cerium oxide catalysts: selective C [double bond, length as m-dash] O bond hydrogen requires platinum sites beyond the oxide–metal interface. Catalysis Science & Technology. 2016;6(18):6824-35.
28. Mueanngern Y, Yang X, Tang Y, Tao FF, Baker LR. Catalysis at Multiple Length Scales: Crotonaldehyde Hydrogenation at Nanoscale and Mesoscale Interfaces in Platinum–Cerium Oxide Catalysts. The Journal of Physical Chemistry C. 2017;121(25):13765-76.
29. Baker R, Barber M, Harris P, Feates F, Waite R. Nucleation and growth of carbon deposits from the nickel catalyzed decomposition of acetylene. Journal of catalysis. 1972;26(1):51-62.

30. Sharma R, Rez P, Treacy MM, Stuart SJ. In situ observation of the growth mechanisms of carbon nanotubes under diverse reaction conditions. Journal of electron microscopy. 2005;54(3):231-7.
31. Sharma R, Rez P, Brown M, Du G, Treacy M. Dynamic observations of the effect of pressure and temperature conditions on the selective synthesis of carbon nanotubes. Nanotechnology. 2007;18(12):125602.
32. Yoshida H, Takeda S, Uchiyama T, Kohno H, Homma Y. Atomic-scale in-situ observation of carbon nanotube growth from solid state iron carbide nanoparticles. Nano letters. 2008;8(7):2082-6.
33. Gohier A, Ewels C, Minea T, Djouadi M. Carbon nanotube growth mechanism switches from tip-to base-growth with decreasing catalyst particle size. Carbon. 2008;46(10):1331-8.
34. Nesbitt H, Legrand D, Bancroft G. Interpretation of Ni2p XPS spectra of Ni conductors and Ni insulators. Physics and Chemistry of Minerals. 2000;27(5):357-66.
35. Gili A, Schlicker L, Bekheet MF, Görke O, Kober D, Simon U, et al. Revealing the mechanism of multiwalled carbon nanotube growth on supported nickel nanoparticles by in situ synchrotron X-ray diffraction, density functional theory, and molecular dynamics simulations. ACS Catalysis. 2019;9(8):6999-7011.
36. Feng X, Chee SW, Sharma R, Liu K, Xie X, Li Q, et al. In Situ TEM observation of the gasification and growth of carbon nanotubes using iron catalysts. Nano Research. 2011;4(8):767.
37. Rümmeli MH, Bachmatiuk A, Börrnert F, Schäffel F, Ibrahim I, Cendrowski K, et al. Synthesis of carbon nanotubes with and without catalyst particles. Nanoscale research letters. 2011;6(1):1-9.
38. Dijon J, Szkutnik P, Fournier A, De Monsabert TG, Okuno H, Quesnel E, et al. How to switch from a tip to base growth mechanism in carbon nanotube growth by catalytic chemical vapour deposition. Carbon. 2010;48(13):3953-63.
39. Liotta L, Ousmane M, Di Carlo G, Pantaleo G, Deganello G, Marcì G, et al. Total oxidation of propene at low temperature over Co3O4–CeO2 mixed oxides: Role of surface oxygen vacancies and bulk oxygen mobility in the catalytic activity. Applied Catalysis A: General. 2008;347(1):81-8.
40. Chen H-L, Chen H-T. Role of hydroxyl groups for the O2 adsorption on CeO2 surface: A DFT+ U study. Chemical Physics Letters. 2010;493(4-6):269-72.
41. Zhang C, Li S, Wu G, Gong J. Synthesis of stable Ni-CeO2 catalysts via ball-milling for ethanol steam reforming. Catalysis Today. 2014;233:53-60.
42. Fu Q, Weber A, Flytzani-Stephanopoulos M. Nanostructured Au–CeO2 catalysts for low-temperature water–gas shift. Catalysis Letters. 2001;77(1):87-95.
43. Shido T, Iwasawa Y. Reactant-promoted reaction mechanism for water-gas shift reaction on Rh-doped CeO2. Journal of Catalysis. 1993;141(1):71-81.
44. Du X, Zhang D, Shi L, Gao R, Zhang J. Morphology dependence of catalytic properties of Ni/CeO2 nanostructures for carbon dioxide reforming of methane. The Journal of Physical Chemistry C. 2012;116(18):10009-16.
45. Wang S, Lu GM. Role of CeO2 in Ni/CeO2–Al2O3 catalysts for carbon dioxide reforming of methane. Applied Catalysis B: Environmental. 1998;19(3-4):267-77.